



HAL
open science

Ridge subduction and afterslip control aftershock distribution of the 2016 Mw 7.8 Ecuador earthquake

H. Agurto-Detzel, Y. Font, P. Charvis, M. Regnier, A. Rietbrock, D. Ambrois, M. Paulatto, A. Alvarado, S. Beck, F. Courboulex, et al.

► **To cite this version:**

H. Agurto-Detzel, Y. Font, P. Charvis, M. Regnier, A. Rietbrock, et al.. Ridge subduction and afterslip control aftershock distribution of the 2016 Mw 7.8 Ecuador earthquake. *Earth and Planetary Science Letters*, 2019, 520, pp.63-76. 10.1016/j.epsl.2019.05.029 . hal-02167273

HAL Id: hal-02167273

<https://hal.science/hal-02167273>

Submitted on 3 Jul 2020

HAL is a multi-disciplinary open access archive for the deposit and dissemination of scientific research documents, whether they are published or not. The documents may come from teaching and research institutions in France or abroad, or from public or private research centers.

L'archive ouverte pluridisciplinaire **HAL**, est destinée au dépôt et à la diffusion de documents scientifiques de niveau recherche, publiés ou non, émanant des établissements d'enseignement et de recherche français ou étrangers, des laboratoires publics ou privés.

Ridge Subduction and Afterslip Control Aftershock 1 Distribution of the 2016 Mw 7.8 Ecuador Earthquake

H. Agurto-Detzel, Y. Font, P. Charvis, M. Régnier, A. Rietbrock, D. Ambrois, M. Paulatto, A. Alvarado, S. Beck, F. Courboulex, L. De Barros, A. Deschamps M.J. Hernandez, S. Hernandez, M. Hoskins, S. León-Ríos, C. Lynner, A. Meltzer, D. Mercerat, F. Michaud, J.M. Nocquet, F. Rolandone, M. Ruiz, L. Soto-Cordero

7

8 Corresponding author: HAD agurto@geoazur.unice.fr h.agurto.detzel@gmail.com

9

10

Abstract

12 We characterise the aftershock sequence following the 2016 Mw=7.8 Pedernales earthquake.

13 More than 10,000 events were detected and located, with magnitudes up to 6.9. Most of the aftershock seismicity results from interplate thrust faulting, but we also observe a few normal and strike-slip mechanisms. Seismicity extends for more than 300 km along strike, and is constrained between the trench and the maximum depth of the coseismic rupture. The most striking feature is the presence of three seismicity bands, perpendicular to the trench, which are also observed during the interseismic period. Additionally, we observe a linear dependency between the temporal evolution of afterslip and aftershocks. We also find a temporal semi-logarithmic expansion of aftershock seismicity along strike and dip directions, further indicating that their occurrence is modulated by afterslip. Lastly, we observe that the spatial distribution of seismic and aseismic slip processes is correlated to the distribution of bathymetric anomalies associated with the northern flank of the Carnegie Ridge, suggesting that slip in the area could be influenced by the relief of the subducting seafloor. To explain our observations, we propose a conceptual model in which the Ecuadorian margin is subject to a bimodal slip mode, with distributed seismic and aseismic slip mechanically controlled by the subduction of a rough oceanic relief. Our study sheds new light on the mechanics of subduction, relevant for convergent margins with a complex and heterogeneous structure such as the Ecuadorian margin.

30 Keywords: Aftershock; Subduction; Afterslip; Ecuador; Carnegie Ridge; Seafloor Relief;

31 **1. Introduction**

32 The largest earthquakes on Earth occur in subduction zones, which also host a diversity of
33 processes including seismic and aseismic slip along the subduction interface (e.g. Bilek and
34 Lay, 2018, and references therein). What controls the occurrence and distribution of these
35 phenomena remains an outstanding problem in Earth sciences. One way to gain a better
36 insight into the nature of the subduction mechanism and the physical medium that host them,
37 is by studying the aftershocks sequence that follows a large megathrust earthquake.
38 Moreover, the high rate of seismicity during aftershock sequences, combined with recent
39 technological and logistical improvements in seismological network deployments and data
40 processing (e.g. Beck et al., 2014), allows us to collect and analyse vast amounts of data with
41 increased spatio-temporal resolution.

42

43 Aftershocks occur either because of the release of residual stresses on the mainshock fault
44 and surrounding medium, or as a result of static or dynamic stress perturbations due to the co-
45 seismic rupture and subsequent aftershocks (e.g. Das and Henry, 2003; Freed, 2005).

46 Consequently, aftershocks can provide an independent constraint in the shape and extension
47 of the rupture area and interface heterogeneities, as well as help us identify areas of partially
48 released and/or accumulated stress over the megathrust interface following the mainshock,
49 thus delineating potential source areas for future earthquakes.

50 The often intricate distribution of aftershocks accounts for a complex distribution of
51 remaining stresses and interface heterogeneities following the mainshock. For instance, after
52 the 2005 Mw=8.7 Nias-Simeulue earthquake in Sumatra, Hsu et al. (2006) found that
53 aftershocks clustered in the boundary area between the coseismic rupture and the afterslip
54 area, with afterslip concentrated mostly up-dip of the coseismic rupture. Furthermore, it is
55 often observed that regions of large co-seismic slip tend to have little seismicity after the

56 mainshock rupture, whilst the largest aftershocks concentrate around the patches of large co-
57 seismic slip (e.g. Das and Henry, 2003; Rietbrock et al., 2012; Agurto et al., 2012; Wetzler et
58 al., 2018). On the other hand, aftershock activity is not only limited to the megathrust
59 interface, but also to the surrounding seismogenic volume, often showing a diversity of focal
60 mechanisms and complex interactions between activity in the slab and in the overriding plate
61 (e.g. Asano et al., 2011). Lastly, for some subduction earthquakes, such as the 2011 Tohoku,
62 Japan earthquake, the reduction of shear stresses after the mainshock is such that it produces
63 a rotation of the deviatoric stress field, potentially causing extensional earthquakes in a
64 previously compressional setting (e.g. Ryder et al., 2012; Hardebeck, 2012).

65

66 Moreover, the physics behind aftershock generation is still not fully understood. Aftershocks
67 were first described and used as a proxy for the mainshock rupture extension, and
68 subsequently explained as ruptures on surrounding faults due to the re-distribution of strain
69 energy following the mainshock. Consequently, aftershocks triggering mechanism would be
70 related to dynamic and/or static stress transfers, following the mainshock and subsequent
71 aftershocks (Stein, 1999). More recently, observational and theoretical studies have proposed
72 that afterslip plays an important role in the occurrence and distribution of aftershocks (e.g.
73 Henry and Das, 2001; Perfettini et al., 2018). For example, following the 2005 Mw=8.7 Nias-
74 Simeulue earthquake in Sumatra, Hsu et al. (2006) found that the cumulative number of
75 aftershocks increased linearly with the postseismic displacement, suggesting that the
76 temporal evolution of aftershocks is governed by afterslip.

77

78 On the 16 of April 2016, a Mw=7.8 earthquake struck the coast of northern Ecuador
79 rupturing a ~100 km-long asperity of the interface between the Nazca plate and South
80 America (Nocquet et al., 2017). Shortly after the mainshock, we deployed an amphibious

81 temporary network of seismic stations to monitor the evolution of the seismic activity. In this
82 paper, we benefit from the continuous seismic waveform dataset acquired during one year of
83 the aftershock deployment to explore the distribution of hypocentral locations and
84 magnitudes for the Pedernales sequence. We also use full waveform inversions to compute
85 moment tensors for a selection of events, providing a seismotectonic constraint to the
86 characterization of the sequence. We discuss our results in the light of the earthquake cycle,
87 exploring the relations between seismic and aseismic processes within the context of a
88 subduction zone with highly heterogeneous frictional properties. Finally, we present a
89 conceptual model in which we explain the distribution and diversity of slip processes in the
90 Ecuadorian margin, and the control factors that affect them.

91

92 *1.1 Seismotectonic context and previous studies*

93 The Ecuador-Colombia subduction margin has generated four large tsunamigenic megathrust
94 earthquakes ($M_w > 7.5$) in the 20th century. In 1906, an $M_w \sim 8.8$ event (the largest thus far
95 documented offshore Ecuador) ruptured a roughly 500 km-long segment of the margin,
96 causing widespread damage and tsunami waves (Kanamori and McNally, 1982). Subsequent
97 events occurred in 1942 ($M_w 7.8$), 1958 ($M_w 7.7$) and 1979 ($M_w 8.2$; Kanamori and
98 McNally, 1982; Beck and Ruff, 1984), partially overlapping the rupture area of the 1906
99 event. This sequence of three earthquakes presented a northward migration pattern (Fig. 1),
100 and the sum of their combined seismic moments accounts for only a fifth of the moment
101 released by the 1906 event (Keller, 1972; Kanamori and McNally, 1982). This would imply
102 that the 1906 event not only ruptured the other three isolated asperities simultaneously, but
103 also broke the adjacent subduction interface which otherwise creeps during the interseismic
104 period.

105

106 The area that ruptured in 2016 had already been identified as a highly coupled region (Chlieh
107 et al., 2014; Nocquet et al., 2014), and the same asperity had allegedly been ruptured by the
108 earthquake of 1942 (Nocquet et al., 2017). In this region, the convergence rate between
109 Nazca and South America is 58 mm/yr, which is partially accommodated by the north-eastern
110 motion of the North-Andean sliver, resulting in a slip rate of 46 mm yr⁻¹ at the megathrust
111 (Chlieh et al., 2014; Nocquet et al., 2014). Also, this area is located within the northern flank
112 of the aseismic Carnegie Ridge (hereafter CR), which currently subducts beneath South
113 America between 0° to 2.5° lat. S.

114

115 To date, several co-seismic slip models of the 2016 earthquake have been published based on
116 a complete or partial use of teleseismic, tsunami, GPS, InSAR and regional accelerometric
117 data (e.g. Ye et al., 2016; Nocquet et al., 2017; Yoshimoto et al., 2017; Gombert et al., 2018
118 and references within). All models have in common an extension of the rupture area of
119 roughly 100 km along strike, a southward propagation rupture, and the presence of two
120 patches of high coseismic slip with no shallow slip near the trench. They differ, however, in
121 the maximum and average amount of slip, with maximum slip ranging from 2 m (Yoshimoto
122 et al., 2017) to 6-7 m (Nocquet et al., 2017; Gombert et al., 2018). These last two models are
123 very similar regarding magnitude and distribution of the co-seismic slip, and are the most
124 comprehensive up to date in terms of diversity of used datasets and methodology.

125

126 Previous studies using geodetic and seismological data highlight the diverse nature of slip
127 processes in the interseismic period. Font et al. (2013) produced a seismicity catalogue for a
128 13-yr period based on locations in a 3-D a priori velocity model. Vallée et al. (2013)
129 characterized a one-week-long slow slip event (SSE), accompanied by a seismic swarm, that
130 occurred in August 2010 below La Plata Island (hereafter LPI), south of the 2016 rupture.

131 Similarly, Vaca et al. (2018) described a six-week-long SSE accompanied by a seismic
132 swarm that occurred between December 2013 and January 2014 at the northern limit of the
133 2016 rupture, arguing that this area acted as a barrier for the 2016 rupture propagation
134 northwards. Finally, Segovia et al. (2018) studied the seismicity distribution during a two-
135 year experiment in the south of the region, describing the interface geometry, and associating
136 swarm-like activity to a SSE below LPI.

137

138 **2. Data and Methods**

139 ***Earthquake rapid response deployment***

140 Following the Pedernales earthquake, an international effort involving institutions from
141 Ecuador (IG-EPN), France (Géoazur, Cerema, IRD and CNRS), the UK (U. of Liverpool)
142 and the USA (IRIS, U. of Lehigh, U. of Arizona) rapidly installed a network of 50 inland
143 stations and 10 ocean-bottom seismometers (OBS) to record for one year after the mainshock
144 (Fig. 2; Meltzer et al., 2018). This temporary deployment complemented the permanent
145 Ecuadorian network (Alvarado et al., 2018). Instruments included broadband, intermediate
146 and short period stations, in addition to some accelerometers from the Ecuadorian network,
147 all recording at a sampling rate of 100 Hz or higher.

148

149 ***Data processing***

150 The continuous waveforms were collected and archived in mini-seed format. They were
151 processed using the software package *SEISCOMP3* (SC3; <https://www.seiscomp3.org>) which
152 provides in-built capacity to detect, associate and locate seismic events including the
153 calculation of magnitudes. Although SC3 is primarily designed for real-time monitoring with
154 continuous injection of data, it can also be used in ‘playback mode’, that is, injecting and
155 processing the whole of the collected data at once. Parameterization of the different SC3

156 modules is critical, and therefore we adopted an empirical approach in which several tests
157 were systematically performed looking for the best set of parameters that would maximize
158 the number of real events while minimizing the number of false detections. Control days, for
159 which we manually detected events, were used to assess this fine-tuning process. Additionally,
160 we visually inspected the detected events and discarded false detections as well as classified
161 real events into first and second quality events according to the number and accuracy of their
162 automatic picks (see Sup. Mat.).

163

164 The workflow was as follows: after injection of the continuous waveform dataset, detection
165 of arrival times was performed using a standard STA/LTA algorithm for P-phases and the
166 AIC picker implemented in SC3 for S-phases, on band-pass filtered waveforms (1-10 Hz for
167 seismometers; 1-8 Hz for accelerometers and OBS). Subsequently, we used the SC3 module
168 *SCANLOC*, which is based on the cluster-search algorithm *DBSCAN* (Easter et al., 1996), to
169 associate picks and locate events. Relocation of these initial events was performed using the
170 *NonLinLoc* (NLL) algorithm (Lomax, 2000) configured in standard global mode. The visual
171 quality-inspection described above was carried out on these preliminary locations. Finally,
172 the whole set of events was relocated outside SC3 using NLL configured in regional mode
173 (Cartesian coordinates) and a simplified velocity model taken from a newly derived 1-D
174 velocity structure for the region (León-Ríos et al., 2017; see Sup. Mat.).

175

176 Initially, a total of 15,233 aftershocks were detected and located for the period between April
177 16 2016 to April 30 2017. Visual analysis of seismic sections was performed to identify and
178 discard false detections, spurious events, and to assess the pick quality to assemble a high-
179 quality subset of events. After this visual inspection, a total of 4,963 (33%) events were

180 discarded as false detections or spurious events (poor signal and/or too noisy). The 10,270
181 events left were classified into two categories according to their picks and location quality:
182 1st quality: events with at least four P-phases and clear arrival picks - 7326 events
183 2nd quality: events with pick residuals larger than ~2 s and greater location errors - 2944
184 events

185

186 ***Moment tensor inversions***

187 We selected aftershocks with $M_L > 4.5$ to compute moment tensors from full waveform
188 inversions, including both body and surface waves. For this we used the software ISOLA
189 (Sokos and Zaharadnik, 2008) which can handle inversions of local to regional waveforms.
190 Green functions were computed using the 1-D model produced by León-Ríos et al. (2017)
191 and waveforms were inverted in the 10 – 25 s period range. Horizontal centroid position was
192 kept fixed to the epicentral position from the earthquake locations, but a grid-search was
193 performed to obtain optimal centroid depth and time. Examples of the inversion and fitting
194 are provided in the Supplementary Material.

195

196 ***Magnitudes***

197 Local magnitudes (M_L) were calculated from maximum P-wave amplitudes on vertical
198 components. The obtained magnitudes vary between 0.7 and 6.9, with a magnitude of
199 completeness $M_c = 2.5$ (Sup. Mat.). In general, there is a good agreement between the
200 calculated local magnitudes (M_L) and the moment magnitudes (M_w) obtained from our
201 moment tensor inversions and those from the GCMT catalogue (Sup. Mat.). Nonetheless, we
202 observe that for $M_w > 5.6$ there is an underestimation of local magnitudes, probably due to
203 saturation of the M_L scale. On the other hand, for $M_w < 5.6$ we observe an overestimation of

204 M_L by ~ 0.3 units. These differences are commonly observed when comparing local
205 magnitudes with moment magnitudes (e.g. Deichmann, 2006).

206

207 ***Residual bathymetry***

208 In order to compare the distribution of seismicity with the distribution of the incoming
209 oceanic relief, we produced a residual bathymetry grid for the Ecuadorian margin following
210 the ensemble averaging approach of Basset and Watts (2015), and using the higher resolution
211 GEBCO2014 grid. We calculated the average topography for a series of trench-normal
212 profiles. Then we subtracted this averaged topography from the original grid to produce an
213 elevation map where large-amplitude trench-normal variations associated with the subduction
214 zone have been removed and short-wavelength/lower amplitude structures are preserved and
215 highlighted.

216

217 **3. Spatio-temporal distribution of aftershocks**

218 Along strike, the aftershock seismicity extends beyond the coseismic rupture, over 300+ km,
219 from latitude 1°N to at least 1.5°S (Fig. 3). Along the dip direction, the seismicity seems to be
220 constrained by the coseismic rupture maximum depth, with most of the aftershocks located in
221 the upper 30 km and no aftershock seismicity locates deeper than the coseismic rupture
222 termination.

223

224 The most striking feature is the presence of three bands of seismicity perpendicular to the
225 trench, and located up-dip west of the mainshock rupture area (profiles BB', CC' and DD' in
226 Fig. 3; see also Soto-Cordero et al., 2017). Interestingly, this seismicity pattern is also
227 observed in the background seismicity during the interseismic period (Font et al., 2013). The
228 northern band (BB') extends for about 40 km up-dip with a width of about 10 km. The

229 central band (CC') is more diffuse, starting at the upper termination of the rupture area and
230 extending 40 km up-dip with a width of around 20 km. The southern band also starts at the
231 upper termination of the coseismic rupture and extends up-dip 60 km with a width of about
232 25 km. Both, the southern and central bands reach the trench, whilst seismicity is more
233 diffuse close to the trench for the northern band. Although we do observe seismicity near the
234 trench, we do not observe any extensional focal mechanism in this area that could be related
235 to outer rise seismicity following the mainshock (e.g. Sladen and Trevisan, 2018).
236 Considering the location uncertainties, most of the seismicity in these three alignments occurs
237 at the interface or within 10 km from it. Additionally, all large aftershocks ($M \geq 5$) occur
238 outside the mainshock rupture and mostly along bands BB' and DD', located up-dip at the
239 northern and southern limits of the co-seismic rupture, respectively. Inside the mainshock
240 rupture area, seismicity occurs mostly between the two patches of maximum coseismic slip
241 (Figure 5, see Section 5).

242

243 To the north (0.9° N), we observe a cluster of seismicity within the subduction interface
244 below the coastline (cluster G1 in Fig. 3). Further to the east, a cluster of crustal seismicity
245 (G2, hereafter called Esmeraldas sequence) is observed at 10-20 km depth. This group of
246 shallow seismicity started to develop at the end of June 2016, with a burst of seismicity
247 during July 5-8 and its largest earthquake, normal faulting $M_w=4.9$, occurring on July 6,
248 2016 (see details in Section 4).

249

250 South of the mainshock rupture area, we observe three separate groups of seismicity. The
251 first one is a cluster of events occurring beneath the coastline, at around latitude 0.9° S (G3).
252 This cluster seems to occur on the megathrust interface, and as seen in Section 4, presents
253 thrust focal mechanisms compatible with subduction earthquakes. The second group

254 corresponds to the seismicity observed inland at around latitude 1.3°S (G4) which also occur
255 at the interface. The third group (G5) is located offshore, nearby LPI. This seismicity is
256 sparsely distributed, and because of its location offshore at the southern end of the network, it
257 is difficult to assess hypocentral depths with certainty. Nevertheless, a clue regarding the
258 origin of this seismicity comes from previous studies which have found swarm-like
259 seismicity and SSEs in this area (Vallee et al., 2013; Segovia et al., 2018), as well as a SSE
260 during the early postseismic period of the 2016 mainshock (Rolandone et al., 2018). Like the
261 trench-normal bands, these three seismicity groups had also been observed during the
262 interseismic period (Segovia et al., 2018).

263

264 The spatio-temporal analysis of the aftershock sequence (Sup. Video) shows that during the
265 first 24 hours after the mainshock, aftershocks start to nucleate mostly along profiles DD' and
266 CC', and in particular between the two patches of maximum co-seismic slip. The aftershocks
267 then extend along profiles BB' and EE'. Seismicity around LPI starts on the third day with
268 peaks of activity on the 11th and 12th days after the mainshock. A last burst of seismicity in
269 this area occurs between 1st and 3rd December 2016. As stated above, the shallow clustered
270 seismicity of the Esmeraldas sequence occurs mostly during early July 2016. Finally, the
271 seismicity observed at the interface along the profile AA' develops during December 2016.

272

273 **4. Seismotectonics and moment tensor inversions**

274 For the 12-month period following the Pedernales mainshock (April 16 2016 – April 30
275 2017) there are 32 moment tensors with Mw between 4.8 and 6.9 available in the GCMT
276 catalogue (<http://www.globalcmt.org/>). We complemented these with 29 additional events
277 with Mw between 4.1 and 5.0, for a total of 61 moment tensors (Fig. 4 and Sup. Mat.). Most
278 of the moment tensors indicate thrust faulting at the subduction interface. No large

279 aftershocks ($M_w > 5$) occur inside the coseismic rupture area. The largest thrust aftershocks
280 occur along the seismicity bands located at the northern and southern termination of the
281 mainshock rupture. Besides these two bands dominated by thrust faulting at the interface,
282 we also observe subduction earthquakes to the south, around latitude 1°S , and towards the
283 north by the coastline up to 1°N . The geometry of the reverse faulting focal mechanisms is
284 similar to that of the mainshock, with an average rotational angle (Kagan angle) of 22°
285 relative to the mainshock's focal mechanism (inset Fig. 4).

286

287 We also observe a few normal and strike-slip events. Strike-slip events seem to be sparsely
288 located and within the subducting slab. A possible explanation for this activity could be the
289 presence of pre-existing structures in the subducting CR, reactivated by the mainshock. On
290 the other hand, two similar normal fault earthquakes, of M_w 5.1 and 4.9 respectively,
291 occurred in the marine forearc around latitude 0.3°N , on June 1st 2016, separated by 5
292 hours. The GCMT centroid depths for these earthquakes (12 and 17 km depth) place them
293 close to the subduction interface, but on our own regional moment tensor inversions we
294 found the lowest waveform misfit at 5 km depth. Despite the depth uncertainties, a possible
295 explanation for this faulting could be given by the existence at this location of a subducted
296 seamount, previously imaged using multi-channel seismic reflection data (Marcaillou et al.,
297 2016). León-Ríos et al. (2017) hypothesize that the subduction of this structure produces an
298 anomalous extensional stress field parallel to the convergence vector, which in turn could
299 have been affected by the 2016 mainshock. In fact, Marcaillou et al. (2016) observed a
300 complex and highly fractured margin structure in this region, and argued that the absence
301 of background seismicity and low interseismic coupling here suggest that this area is

302 incapable of storing sufficient elastic strain to produce large thrust earthquakes and
303 tsunamis.

304

305 Two additional normal fault events are observed in our dataset. One is a $M_w=4.4$
306 intermediate-depth event, most likely intra-slab, located at 0.6°N , 200 km east of the
307 trench. The other is a $M_w=4.9$, crustal normal fault event with a strike-slip component,
308 belonging to the Esmeraldas sequence. Unfortunately, the uncertainties of our hypocentral
309 locations in this area do not allow us to distinguish the fault plane from the two nodal
310 planes. On the other hand, the geological map for this area (Reyes and Michaud, 2012; Sup.
311 Mat.) shows a set of normal faults striking ESE and dipping to the S, which coincide with one
312 of the nodal planes of this event (strike 103, dip 42, rake -29). We suggest that crustal
313 activity on one of these faults might be responsible for the seismicity observed during the
314 Esmeraldas sequence (see also Hoskins et al., 2018). Some previous large megathrust
315 aftershock sequences, such as Maule 2010 and Tohoku 2011, have shown similar shallow
316 normal faulting at the edges of the coseismic rupture area (e.g. Kato et al., 2011; Ryder et
317 al., 2012). A similar tectonic configuration could be responsible for our normal event in the
318 Esmeraldas area, which indicates horizontal extension in the overriding plate following the
319 mainshock. Since these events are shallow, near the coast, and can produce considerable
320 vertical displacement, they are important to consider when estimating earthquake and
321 tsunami hazard at a local scale.

322

323 *The April 16 2016 $M_w=4.9$ foreshock*

324 Nearly 11 minutes before the Pedernales earthquake, an event $M_w=4.9$ nucleated about 14
325 km ESE of the mainshock's epicentre. We also obtained the moment tensor for this event,

326 which indicates a thrust faulting mechanism, likely on the subduction interface (Fig. 4). The
327 possibility of this earthquake to have triggered the $M_w=7.8$ mainshock is worth exploring,
328 although a dynamic or static triggering would be difficult to reconcile with the time and
329 distance between the two events. More accurate relocations of both the foreshock and main
330 event hypocentres, and a detailed analysis of the Coulomb stress change field, beyond the
331 scope of this study, would be necessary to resolve this issue.

332

333 **5. Relation between coseismic rupture and aftershock distribution**

334 As a first order feature, we observe an inverse correlation between the number of aftershocks
335 and co-seismic slip, with highs in slip associated to lows in seismicity and vice versa (e.g. at
336 20, 45 and 60 km south of the mainshock in profile N-S of Fig. 3). Figure 5 shows in detail
337 the distribution of aftershocks and co-seismic slip. We observe that most of the large
338 aftershocks occur outside the mainshock rupture area (defined as the 1 m slip contour area).
339 When we consider all magnitudes, 28% of the aftershocks occur inside the mainshock
340 rupture, but when we consider only events with $M_L \geq 3.5$, only 14% of aftershocks nucleate
341 inside and, moreover, no aftershock larger than $M_L=5$ nucleated inside the mainshock rupture
342 area.

343

344 Additionally, the histograms in Fig. 5 show the normalized areal distribution of co-seismic
345 slip together with the normalized frequency distribution of aftershocks inside the coseismic
346 rupture. Accordingly, if the aftershocks occurrence were randomly distributed, the aftershock
347 frequency curve would resemble the slip frequency distribution. Instead, we observe that
348 aftershocks tend to concentrate at intermediate levels of coseismic slip (2 - 3.5 m),
349 particularly in areas of large slip gradient, such as in between the two patches of coseismic
350 slip maxima. On the other hand, areas of low coseismic slip (< 2 m) present less seismicity

351 than expected, whilst areas of high coseismic slip (> 4.5 m) seem to present a random
352 distribution of aftershocks (histogram Fig. 5a), although when we consider only events with
353 $M_L \geq 3.5$, there is a lack of aftershocks compared to a random distribution (histogram Fig. 5b).

354

355 If we look at the aftershock density, we observe that in terms of number of events, the highest
356 density is located inside the mainshock rupture area, in between the two patches of maximum
357 coseismic slip (Fig. 6a). If instead we look at the seismic moment density (Fig. 6b), we
358 observe that inside the mainshock rupture area the moment density is relatively low ($< 1e^{17}$ N
359 m / $0.1^\circ \times 0.1^\circ$). On the other hand, high moment density ($> 1e^{18}$ N m / $0.1^\circ \times 0.1^\circ$) is observed
360 outside the mainshock rupture, along the three trench-normal seismicity bands and
361 particularly nearby the coastline at latitude 0.5° N, due to the occurrence here of the largest
362 aftershock of the sequence ($M_w=6.9$, thrust faulting).

363

364 **6. Relation between seismic and aseismic processes**

365 We compare the temporal evolution of the aftershock sequence with that of the geodetic
366 afterslip during the first 30 days following the mainshock. Following Rolandone et al. (2018),
367 we consider the afterslip and aftershocks as three discrete patches (North, South and LPI; see
368 Fig. 3 and Sup. Mat) according to their spatial distribution, and analyse them separately (Fig.
369 7). Cumulative seismicity (red curve) for the northern and southern patches show an Omori-
370 type decay in which a steep slope is observed immediately after the mainshock, followed by a
371 deceleration after the first week of aftershocks. On the other hand, the LPI patch shows a
372 rather slow start in aftershocks generation, and then an increase from day 8 until day ~ 20
373 when it decreases again. The different behaviour in the LPI patch could be explained because
374 this area hosted a slow slip event associated to seismicity during this period (Rolandone et al.,
375 2018).

376 We observe for all three patches that the curve for cumulative number of earthquakes closely
377 follows that of the afterslip cumulative moment release, implying a linear relationship
378 between both processes. In fact, if we assume that both afterslip and aftershocks cumulative
379 distributions present an exponential behaviour, their curves should resemble a straight-line in
380 a semi-logarithmic plot, as seen in the right panels of Fig. 7, which also show both curves
381 present similar slopes (segmented lines). Leaving the LPI patch aside, the linear relation
382 between cumulative aftershocks and afterslip release is remarkable.

383

384 Furthermore, for each of the patches we observe that after 30 days of postseismic activity, the
385 total cumulative moment released by the aftershocks represents about 10% of the cumulative
386 moment released by the afterslip, indicating that most of the postseismic deformation is
387 aseismic (Sup. Mat).

388

389 Additionally, we explore the spatial dependency between afterslip and aftershocks. As seen
390 from the geographic distribution of seismicity outside the mainshock rupture area,
391 aftershocks are spatially associated with afterslip, particularly in the area of the trench-normal
392 bands and around LPI (Fig. 3). Figure 8 shows the temporal evolution of seismicity as a
393 function of along-strike distance from the mainshock epicentre, clearly showing a log-time
394 expansion of the aftershocks. A similar behaviour is seen for the along-dip direction (Sup.
395 Mat). These observations are consistent with previous studies (e.g. Frank et al., 2017), and
396 numerical modelling (e.g. Ariyoshi et al., 2007; Perfettini et al., 2018) which suggest that this
397 type of semilogarithmic migration is indicative of afterslip-driven aftershock activity.

398

399

400

401 **7. Discussion**

402 *7.1 Where do aftershocks occur?*

403 The largest aftershocks occur outside the mainshock rupture area. This finding is in
404 agreement with previous studies which have found that regions of high coseismic slip are
405 mostly devoid of large aftershocks, whilst post-seismic seismicity tends to concentrate at the
406 edges of the coseismic rupture (e.g. Das and Henry, 2003; Asano et al., 2011; Rietbrock et
407 al., 2012; Agurto et al., 2012; Frank et al., 2017; Wetzler et al., 2018). For the 2010 Mw=8.8
408 Maule earthquake, Agurto et al. (2012) also found that aftershocks concentrated at
409 intermediate levels of coseismic slip, with areas of low and large coseismic slip lacking in
410 aftershocks. Therefore, this could be a common feature for large megathrust earthquakes with
411 a heterogeneous distribution of coseismic slip.

412

413 Additionally, a large number of aftershocks do occur within the co-seismic rupture area,
414 although presenting low magnitudes. The fact that aftershocks nucleate inside the mainshock
415 rupture area indicates that the accumulated strain energy within the fault is not totally
416 released during the mainshock, or at least that this release is not homogeneously distributed
417 along the megathrust rupture. Attempting to investigate this issue, Yabe and Ide (2018)
418 produced quasi-dynamic numerical simulations in which they replicate several megathrust
419 frictional scenarios and mainshock ruptures with their respective aftershock sequences. They
420 observed aftershocks around and within the mainshock rupture area for cases in which
421 frictional heterogeneity varies significantly along the fault. On the other hand, aftershocks
422 were not produced when frictional heterogeneities along the fault were small. Similarly, the
423 fact that for the Pedernales sequence we observe the highest density of aftershocks within the
424 mainshock rupture area, might be indicative of the highly heterogeneous distribution of
425 frictional properties along the northern Ecuador megathrust.

426 When we account for location uncertainties, the low-magnitude seismicity located within the
427 co-seismic rupture area seems to occur distributed within the seismogenic volume and not
428 only at the megathrust interface (Fig. 3). This volume represents the off-fault damage zone
429 produced by successive megathrust ruptures, and it usually concentrates a diversity of
430 aftershocks focal mechanisms in structures re-activated by the mainshock (e.g. Asano et al.,
431 2011; Agurto et al., 2012).

432

433 *7.2 What controls the evolution of the aftershock seismicity?*

434 The temporal linear dependency between afterslip and aftershocks shown here (Fig. 7)
435 suggests a causative time-based relationship between these two processes, and therefore the
436 temporal distribution of aftershocks associated to patches of afterslip would be modulated by
437 the stressing rate associated with afterslip (e.g. Perfettini and Avouac, 2004; Hsu et al.,
438 2006).

439

440 Additionally, the semi-logarithmic migration of aftershocks both along strike and dip (Fig. 8)
441 suggests that afterslip also controls the spatial extension and migration speed of aftershocks
442 (e.g. Frank et al., 2017; Perfettini et al., 2018). We notice that the origin of the two red lines
443 indicating the propagation front in Fig. 8 is not located at the epicentre but approximately 40
444 km south of it, in the area where most of the aftershock seismicity take place during the first
445 24 hours following the mainshock (Section 3). This corresponds to the centre of the
446 coseismic rupture, and therefore we hypothesize that the expansion of aftershocks is initiated
447 at this point, subsequently propagating outwards.

448

449 Another explanation for the observed aftershocks expansion could be related to fluid
450 diffusion. Nevertheless, in such a case we would observe that the distance D associated with

451 the migration front of the seismicity is related to time t as $D \sim \sqrt{t}c$, where c is the hydraulic
452 diffusivity coefficient (Wang, 2000). This is unlike our observations, in which we see that
453 $D \sim \log(t)$.

454

455 Finally, we notice that a similar relationship between seismic and aseismic processes in our
456 study area has also been described during the interseismic period (Vallée et al., 2013;
457 Rolandone et al., 2018; Segovia et al., 2018; Vaca et al., 2018). These previous studies
458 describe seismic swarms associated to SSEs in the offshore area in front of Punta Galera (lat.
459 $\sim 0.7^\circ\text{N}$; Vaca et al., 2018), and around LPI (Vallée et al., 2013; Segovia et al., 2018). A
460 similar SSE around LPI occurred during the postseismic period of the 2016 Pedernales
461 earthquake, also associated with seismicity (Rolandone et al., 2018). Therefore, it seems that
462 the close spatio-temporal correlation between seismic and aseismic processes in this region is
463 persistent during the whole of the earthquake cycle.

464

465 *7.3 Persistent seismicity patterns over the earthquake cycle*

466 Aseismic slip seems to modulate the rate and spatio-temporal expansion of the aftershock
467 seismicity. But why do these slip processes occur where they occur in the first place? In our
468 study area, the presence of persistent spatial seismicity patterns over the earthquake cycle,
469 such as the three trench-normal bands and the seismicity south of the mainshock rupture area
470 (Font et al., 2013), suggest that earthquake nucleation in these areas is somehow controlled
471 by long-lived structural features. We also notice that the bands are dominated by thrust events
472 (Fig. 4), and oriented perpendicular to the trench, similar to the slip vector of the mainshock,
473 as opposed to parallel to the convergence vector.

474

475 To our knowledge, no other subduction zone presents this type of permanent seismicity
476 pattern transcending the earthquake cycle. Observations in other tectonic settings such as
477 Parkfield, in the San Andreas fault, show sub-horizontal alignments of seismicity along the
478 fault plane that also persist through many seismic cycles. Because of its geometry and the
479 motion of the fault, it has been proposed that this seismic activity is related to rheological
480 transitions within the fault zone and/or stress concentrations between locked and creeping
481 areas (e.g. *Waldhauser et al.*, 2004). Nonetheless, invoking rheological transitions in our area
482 is a less plausible hypothesis to explain our observations, mainly because the seismicity
483 within the bands lacks any clear depth-dependency.

484

485 One additional hypothesis is that the interface frictional properties in these regions of high
486 seismicity are somehow different than in the rest of the area. In this sense, the interseismic
487 coupling map for our study region (Fig. 1) shows that the general area of the bands is only
488 slightly coupled (<40%), but the model lacks the resolution to see any difference along strike,
489 between areas with seismicity (bands) and areas without.

490

491 ***7.4 Influence of the subducting seafloor relief***

492 Previous studies have proposed an along-strike segmentation of the Ecuadorian margin in
493 which large subduction earthquakes only occur north of the CR, which acts as a barrier to the
494 southward propagation of megathrust ruptures (e.g. *Collot et al.*, 2004). More generally, it has
495 been proposed that rugged subducting seafloor, as in the case of seamounts and ridges, give
496 rise to heterogeneous stresses, promoting creep as expressed in transient events of various
497 spatial and temporal scales, accompanied with small and medium-sized earthquakes (*Wang*
498 *and Bilek*, 2014). *Bassett and Watts* (2015) produced a compilation of residual bathymetric
499 anomalies for several subduction zones of the world, and found that regions with subducted

500 seamounts were correlated to reduced levels of megathrust activity, suggesting that these
501 areas are mostly associated with small earthquakes and creep rather than with large
502 megathrust events. Furthermore, they argue that larger bathymetric features, such as aseismic
503 ridges, exhibit seafloor roughness over a larger scale than subducted seamounts, presenting
504 widths comparable to the rupture length of large ($M_w \sim 7$) megathrust earthquakes. They
505 observe that the maximum roughness is located at the flanks of the ridges, which often serve
506 as barriers of rupture propagation. For the Ecuador subduction zone, some authors observed
507 that the northern flank of the CR has acted as a barrier against the southward propagation of
508 the 1906 and 1942 earthquakes (Kelleher, 1972; Collot et al., 2004).

509

510 Following the ensemble averaging approach of Bassett and Watts (2015), and benefiting from
511 combined high resolution datasets, we produced improved maps of residual bathymetry for
512 the Ecuadorian margin. We compared the spatial distribution of these anomalies with the
513 distribution of the seismic and aseismic processes before and after the Pedernales earthquake
514 (Fig. 9). Landward from the trench, the down-dip limit of the area with high residual
515 bathymetry (>2 km) coincides with the up-dip limit of the Pedernales earthquake rupture
516 area. Bassett and Watts (2015) notice that this limit coincide with the continental slope break,
517 and suggest that the slope break corresponds to the updip limit of the seismogenic zone, and
518 that the outer portion of the plate interface, below the steep continental slope, is
519 weak/conditionally stable and would slip aseismically. Furthermore, we notice that both the
520 1942 and the 2016 epicentres are located nearby this limit, with the 2016 mainshock rupture
521 area itself extending down-dip from this limit, within an area of smoother residual
522 bathymetry. We also notice that the trench-normal bands of seismicity observed during the
523 interseismic and post-seismic periods occur in areas of higher gradient and residual
524 bathymetry. In particular, the seismicity band DD', which marks the southern boundary of

525 the Pedernales rupture zone, is in front of the highest bathymetric and gravity anomaly,
526 which correspond to the thickest part of the CR crust (~20 km; Collot et al., 2004; Sallarès et
527 al., 2005). Lastly, both the SSEs observed during the interseismic period, and the afterslip
528 patches observed during the post-seismic period occur in areas dominated by high residual
529 bathymetry due to the subduction of the CR (Fig. 9).

530

531 We summarize our observations in an interpretative figure (Fig. 10) in which we suggest that
532 the Ecuadorian margin hosts a bimodal slip mode mechanically controlled by the distribution
533 of the subducting oceanic relief. The bimodal slip mode produces seismic and aseismic slip
534 processes, and is present both along-strike and along-dip. In the area where the CR subducts
535 beneath the margin (latitude 0° to ~2.5°S), particularly in the region containing a high
536 residual bathymetry (>2 km, from the trench until ~90 km landward; Zone A in Fig. 10), the
537 overall ISC is low (<40%), and the subduction slip mode is dominated by creep and small to
538 medium-sized earthquakes ($M_w < 6$), swarm-like seismicity and SSEs during the interseismic
539 phase, and aseismic afterslip during the postseismic period. Down-dip of this limit (i.e. over
540 90 km horizontally from the trench, down to the maximum seismogenic depth; Zone B), the
541 ISC is higher (>40%) and the slip mode is dominated by large subduction earthquakes
542 ($M_w > 7$) as in the case of the 2016 Pedernales Earthquake and similar past ruptures. Along
543 strike to the north of the ridge flank, away from the area of influence of the CR (Zone C), the
544 overall ISC is high up to the trench, and megathrust earthquake ruptures could reach the
545 trench, as allegedly was the case for the 1906 earthquake and possibly the 1979 earthquake.
546 Therefore, Zone A presents an overall stable regime (velocity-strengthening) whilst Zones B
547 and C are unstable/conditionally stable (velocity-weakening). Thus, the area of high residual
548 bathymetry (> 2 km) would act as a barrier to up-dip (trench-normal) propagation of

549 megathrust ruptures, whilst the lateral flanks of the ridge would act as barriers to along-strike
550 (trench-parallel) rupture propagation.

551

552 **8. Conclusion**

553 We characterised the aftershock seismicity occurring in the Ecuadorian margin over one year
554 following the 2016 $M_w=7.8$ Pedernales earthquake. More than 10,000 events were detected
555 and located, with magnitudes up to 6.9. Most of the seismicity results from interplate thrust
556 faulting but we also observe a few normal and strike-slip mechanisms. Within the mainshock
557 rupture area, seismicity concentrates in regions of intermediate coseismic slip, particularly in
558 between the two patches of slip maxima. Outside the rupture area, seismicity extends for
559 more than 300 km along strike. The most striking feature is the presence of three seismicity
560 bands, perpendicular to the trench, which are also observed during the interseismic period.

561

562 We observe a linear dependency between the temporal evolution of afterslip and number of
563 aftershocks, confirming previous results (Rolandone et al., 2018). Additionally, aftershocks
564 present a temporal semi-logarithmic expansion along the strike and dip directions, which
565 further suggest their spatio-temporal occurrence is regulated by afterslip. A comparison of the
566 distribution of seismic and aseismic slip processes with the distribution of bathymetric
567 anomalies reveals that slip in the area seems to be controlled by the subduction of oceanic
568 plate roughness. To explain our observations, we propose a conceptual model in which the
569 Ecuadorian margin presents a bimodal slip mode mechanically controlled by the subduction
570 of a rough oceanic relief. In this sense, the flanks of the CR act as a barrier to the propagation
571 of megathrust ruptures, both up-dip and along-strike. On the other hand, the area of
572 maximum influence of the CR (residual bathymetry > 2 km) is characterized by small
573 magnitude earthquakes ($M_w < 6$), aseismic slip, repeating events and earthquake swarms.

574 **Acknowledgments**

575 The rapid deployment of the seismic array after the Pedernales earthquake was supported by
576 IG-EPN and IRD in the frame of the International Joint Laboratory “Earthquakes and
577 Volcanoes in the Northern Andes”, INSU-CNRS, the University of Liverpool, Lehigh
578 University and the University of Arizona. The US Seismic Rapid Response deployment was
579 supported by the NSF RAPID Program Award EAR-1642498 and by the PASSCAL facility
580 of the Incorporated Research Institutions for Seismology (IRIS) through the PASSCAL
581 Instrument Center at New Mexico Tech with support from the National Science Foundation
582 under Cooperative Agreement EAR-1261681 and by the Department of Energy National
583 Nuclear Security Administration. The OBS were deployed from R/V "ORION" provided by
584 INOCAR (May 2016) and recovered from Coast Guard vessel "LG-52" in harsh sea
585 conditions thanks to Davide Oregioni and Deny Malengros (Géoazur). A special thank to
586 Comandante Andres Pazmiño (INOCAR) and Esmeraldas Coast-Guard Captain Patricio
587 Estupinian for securing shiptime and providing invaluable help to prepare OBS on-land. We
588 are also grateful to IRD for supporting the postdoc grant of HAD and project REMAKE
589 (ANR-15-CE04-0004) for supporting the processing and interpretation of the data. HAD
590 acknowledges fruitful discussions with I. Manighetti and C. Twardzik. Figures were
591 compiled using GMT software (Wessel and Smith, 1998).

592
593
594
595

References

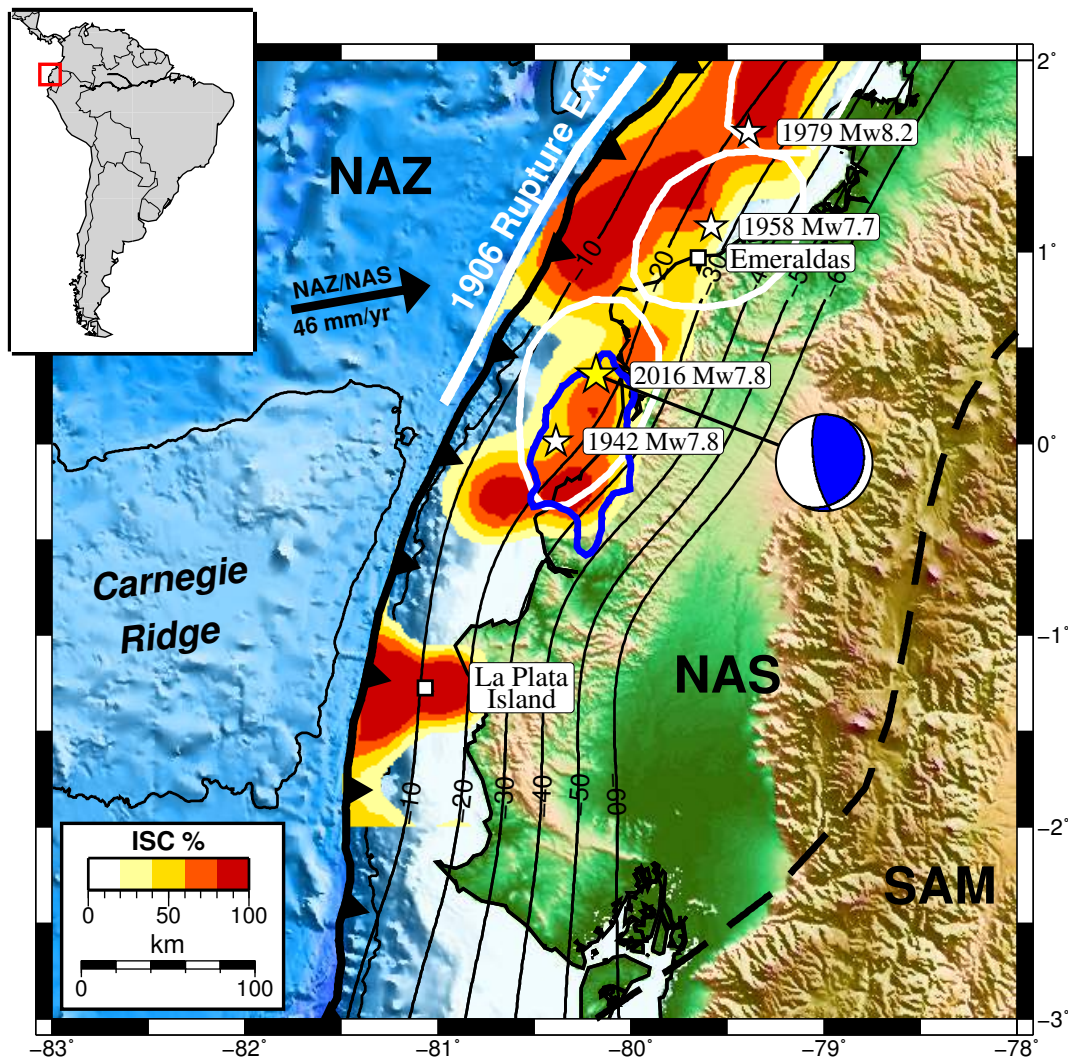
- 596 Agurto, H., Rietbrock, A., Ryder, I., Miller, M., 2012. Seismic-afterslip characterization of
597 the 2010 Mw 8.8 Maule, Chile, earthquake based on moment tensor inversion. *Geophys.*
598 *Res. Lett.* 39. <https://doi.org/10.1029/2012GL053434>
- 599 Alvarado, A., Ruiz, M., Mothes, P., Yepes, H., Segovia, M., Vaca, M., Ramos, C., Enríquez,
600 W., Ponce, G., Jarrín, P., Aguilar, J., Acero, W., Vaca, S., Singaicho, J.C., Pacheco, D.,
601 Córdova, A., 2018. Seismic, Volcanic, and Geodetic Networks in Ecuador: Building
602 Capacity for Monitoring and Research. *Seismol. Res. Lett.* 89.
603 <https://doi.org/10.1785/0220170229>
- 604 Ariyoshi, K., Matsuzawa, T., Hasegawa, A., 2007. The key frictional parameters controlling
605 spatial variations in the speed of postseismic-slip propagation on a subduction plate
606 boundary. *Earth Planet. Sci. Lett.* 256, 136–146.
607 <https://doi.org/10.1016/j.epsl.2007.01.019>
- 608 Asano, Y., Saito, T., Ito, Y., Shiomi, K., Hirose, H., Matsumoto, T., Aoi, S., Hori, S.,
609 Sekiguchi, S., 2011. Spatial distribution and focal mechanisms of aftershocks of the
610 2011 off the Pacific coast of Tohoku Earthquake. *Earth, Planets Sp.* 63, 669–673.
611 <https://doi.org/10.5047/eps.2011.06.016>
- 612 Basset, D., Watts, A., 2015. Gravity anomalies, crustal structure, and seismicity at subduction
613 zones: 1. Seafloor roughness and subducting relief. *Geochemistry Geophys. Geosystems*
614 16, 1508–1540. <https://doi.org/10.1002/2014GC005684>
- 615 Beck, S.L., Ruff, L.J., 1984. The rupture process of the great 1979 Colombia earthquake:
616 evidence for the asperity model. *J. Geophys. Res.* 89, 9281–9291.
617 <https://doi.org/10.1029/JB089iB11p09281>

- 618 Beck, S.L., Rietbrock, A., Tilmann, F., Barrientos, S., Meltzer, A.S., Oncken, O., Bataille,
619 K., Roeker, S., Vilotte, J.-P., Russo, R.M., 2014. Advancing Subduction Zone Science
620 After a Big Quake Access and Use of Data Lead to Innovative Ways. *EOS, Trans. Am.*
621 *Geophys. Union* 95, 193–194.
- 622 Bilek, S.L., Lay, T., 2018. Subduction zone megathrust earthquakes. *Geosphere* 14, 1–33.
623 <https://doi.org/10.1130/GES01608.1>
- 624 Chlieh, M., Mothes, P.A., Nocquet, J.M., Jarrin, P., Charvis, P., Cisneros, D., Font, Y.,
625 Collot, J.Y., Villegas-Lanza, J.C., Rolandone, F., Vallée, M., Regnier, M., Segovia, M.,
626 Martin, X., Yepes, H., 2014. Distribution of discrete seismic asperities and aseismic slip
627 along the Ecuadorian megathrust. *Earth Planet. Sci. Lett.* 400, 292–301.
628 <https://doi.org/10.1016/j.epsl.2014.05.027>
- 629 Collot, J.Y., Marcaillou, B., Sage, F., Michaud, F., Agudelo, W., Charvis, P., Graindorge, D.,
630 Gutscher, M.A., Spence, G., 2004. Are rupture zone limits of great subduction
631 earthquakes controlled by upper plate structures? Evidence from multichannel seismic
632 reflection data acquired across the northern Ecuador-southwest Colombia margin. *J.*
633 *Geophys. Res. Solid Earth* 109, 1–14. <https://doi.org/10.1029/2004JB003060>
- 634 Das, S., Henry, C., 2003. Spatial relation between main earthquake slip and its aftershock
635 distribution. *Rev. Geophys.* 41. <https://doi.org/10.1029/2002RG000119>
- 636 Deichmann, N., 2006. Local Magnitude, a Moment Revisited. *Bull. Seismol. Soc. Am.* 96,
637 1267–1277. <https://doi.org/10.1785/0120050115>
- 638 Ester, M., Kriegel, H., Sander, J., Xu, X., 1996. A Density-Based Algorithm for Discovering
639 Clusters in Large Spatial Databases with Noise. *KDD 96*, 226–231.
- 640 Font, Y., Segovia, M., Vaca, S., Theunissen, T., 2013. Seismicity patterns along the
641 ecuadorian subduction zone: New constraints from earthquake location in a 3-D a priori
642 velocity model. *Geophys. J. Int.* 193, 263–286. <https://doi.org/10.1093/gji/ggs083>
- 643 Frank, W.B., Poli, P., Perfettini, H., 2017. Mapping the rheology of the Central Chile
644 subduction zone with aftershocks. *Geophys. Res. Lett.* 44, 5374–5382.
645 <https://doi.org/10.1002/2016GL072288>
- 646 Freed, A.M., 2005. Earthquake Triggering By Static, Dynamic, and Postseismic Stress
647 Transfer. *Annu. Rev. Earth Planet. Sci.* 33, 335–367.
648 <https://doi.org/10.1146/annurev.earth.33.092203.122505>
- 649 Gombert, B., Duputel, Z., Jolivet, R., Simons, M., Jiang, J., Liang, C., Fielding, E.J., Rivera,
650 L., 2018. Strain budget of the Ecuador–Colombia subduction zone: A stochastic view.
651 *Earth Planet. Sci. Lett.* 498, 288–299. <https://doi.org/10.1016/j.epsl.2018.06.046>
- 652 Hardebeck, J.L., 2012. Coseismic and postseismic stress rotations due to great subduction
653 zone earthquakes. *Geophys. Res. Lett.* 39, 1–6. <https://doi.org/10.1029/2012GL053438>
- 654 Hoskins, M., Meltzer, A., Soto-Cordero, L., Stachnik, J., Beck, S., Lynner, C., Ruiz., M.C.,
655 Alvarado, A., Hernandez, S., Charvis, P., Font, Y., Nocquet, J.M., Rolandone, F.,

- 656 Regnier, M., Agurto-Detzel, H., León-Ríos, S., Rietbrock, A., 2018. Variable Slip
657 Modes in Postseismic Deformation North of the April 16, 2016 M_w 7.8 Pedernales,
658 Ecuador Megathrust Earthquake. Abstract [T43E-0444](#) *2018 Fall Meeting, AGU*,
659 Washington, D.C., 10-14 Dec.
- 660 Hsu, Y.J., Simons, M., Avouac, J.P., Galetka, J., Sieh, K., Chlieh, M., Natawidjaja, D.,
661 Prawirodirdjo, L., Bock, Y., 2006. Frictional afterslip following the 2005 Nias-Simeulue
662 earthquake, Sumatra. *Science* (80-.). 312, 1921–1926.
663 <https://doi.org/10.1126/science.1126960>
- 664 Kanamori, H., McNally, K.C., 1982. Variable rupture mode of the subduction zone along the
665 Ecuador-Colombia coast. *Bull. Seismol. Soc. Am.* 72, 1241–1253.
- 666 Kato, A., Sakai, S., Obara, K., 2011. A normal-faulting seismic sequence triggered by the
667 2011 off the Pacific coast of Tohoku Earthquake: Wholesale stress regime changes in
668 the upper plate. *Earth, Planets Sp.* 63, 745–748. <https://doi.org/10.5047/eps.2011.06.014>
- 669 Kelleher, J.A., 1972. Rupture zones of large South American earthquakes and some
670 predictions. *J. Geophys. Res.* 77, 2087. <https://doi.org/10.1029/JB077i011p02087>
- 671 Leon-Rios, S., Aguiar, A.L., Bie, L., Edwards, B., Velasco, A.J.F., Holt, J., Garth, T.,
672 González, P.J., Rietbrock, A., Agurto-Detzel, H., Charvis, P., Font, Y., Nocquet, J.M.,
673 Regnier, M., Renouard, A., Mercerat, D., Permoud, M., Beck, S., Meltzer, A., Soto-
674 Cordero, L., Alvarado, A., Perrault, M., Ruiz, M. and Santo, J., 2017. The 2016 Mw
675 7.8 Pedernales, Ecuador earthquake: Minimum 1D Velocity Model and Regional
676 Moment Tensors Based on the Aftershock Sequence. Abstract [S53C-2352](#) presented at
677 *2017 Fall Meeting, AGU*, New Orleans, LA, 11-15 Dec.
- 678 Lomax, A., Virieux, J., Volant, P., Berge-Thierry, C., 2000. Probabilistic Earthquake
679 Location in 3D and Layered Models, in: Thurber, C.H., Rabinowitz, N. (Eds.),
680 *Advances in Seismic Event Location*. Kluwer Academic Publishers, pp. 101–134.
681 https://doi.org/10.1007/978-94-015-9536-0_5
- 682 Marcaillou, B., Collot, J.Y., Ribodetti, A., d'Acremont, E., Mahamat, A.A., Alvarado, A.,
683 2016. Seamount subduction at the North-Ecuadorian convergent margin: Effects on
684 structures, inter-seismic coupling and seismogenesis. *Earth Planet. Sci. Lett.* 433, 146–
685 158. <https://doi.org/10.1016/j.epsl.2015.10.043>
- 686 Meltzer A., S. Beck, M. Ruiz, M. Hoskins, L. Soto-Cordero, J.C. Stachnik, C. Lynner, R.
687 Porritt, D. Portner, A. Alvarado, S. Hernandez, H. Yepes, P. Charvis, Y. Font, M.
688 Regnier, A. Rietbrock, 2018. The 2016 Mw 7.8 Pedernales Earthquake, Ecuador:
689 RAPID Response Deployment. *Submitted*.
- 690 Nocquet, J.M., Jarrin, P., Vallée, M., Mothes, P.A., Grandin, R., Rolandone, F., Delouis, B.,
691 Yepes, H., Font, Y., Fuentes, D., Régnier, M., Laurendeau, A., Cisneros, D., Hernandez,
692 S., Sladen, A., Singaicho, J.C., Mora, H., Gomez, J., Montes, L., Charvis, P., 2017.
693 Supercycle at the Ecuadorian subduction zone revealed after the 2016 Pedernales
694 earthquake. *Nat. Geosci.* 10, 145–149. <https://doi.org/10.1038/ngeo2864>

- 695 Nocquet, J.M., Villegas-Lanza, J.C., Chlieh, M., Mothes, P.A., Rolandone, F., Jarrin, P.,
696 Cisneros, D., Alvarado, A., Audin, L., Bondoux, F., Martin, X., Font, Y., Régnier, M.,
697 Vallée, M., Tran, T., Beauval, C., Maguiña Mendoza, J.M., Martinez, W., Tavera, H.,
698 Yepes, H., 2014. Motion of continental slivers and creeping subduction in the northern
699 Andes. *Nat. Geosci.* 7, 287–291. <https://doi.org/10.1038/ngeo2099>
- 700 Perfettini, H., Avouac, J., 2004. Postseismic relaxation driven by brittle creep: A possible
701 mechanism to reconcile geodetic measurements and the decay rate of aftershocks,
702 application to the Chi-Chi earthquake, Taiwan 109, 1–15.
703 <https://doi.org/10.1029/2003JB002488>
- 704 Perfettini, H., Frank, W.B., Marsan, D., Bouchon, M., 2018. A Model of Aftershock
705 Migration Driven by Afterslip. *Geophys. Res. Lett.* 45, 2283–2293.
706 <https://doi.org/10.1002/2017GL076287>
- 707 Reyes, P., Michaud, F., 2012. Mapa Geológico de la Margen Costera Ecuatoriana (1:50000).
708 EP PetroEcuador, Quito, Ecuador.
- 709 Rietbrock, A., Ryder, I., Hayes, G., Haberland, C., Comte, D., Roecker, S., Lyon-Caen, H.,
710 2012. Aftershock seismicity of the 2010 Maule Mw=8.8, Chile, earthquake: Correlation
711 between co-seismic slip models and aftershock distribution? *Geophys. Res. Lett.* 39, 2–
712 6. <https://doi.org/10.1029/2012GL051308>
- 713 Rolandone, F., Nocquet, J.M., Mothes, P.A., Jarrin, P., Vallée, M., Cubas, N., Hernandez, S.,
714 Plain, M., Vaca, S., Font, Y., 2018. Areas prone to slow slip events impede earthquake
715 rupture propagation and promote afterslip. *Sci. Adv.* 4, 2–9.
716 <https://doi.org/10.1126/sciadv.aao6596>
- 717 Ryder, I., Rietbrock, A., Kelson, K., Bürgmann, R., Floyd, M., Socquet, A., Vigny, C.,
718 Carrizo, D., 2012. Large extensional aftershocks in the continental forearc triggered by
719 the 2010 Maule earthquake, Chile. *Geophys. J. Int.* 188, 879–890.
720 <https://doi.org/10.1111/j.1365-246X.2011.05321.x>
- 721 Sallarès, V., Charvis, P., Flueh, E.R., Bialas, J., Party, S.S., 2005. Seismic structure of the
722 Carnegie ridge and the nature of the Galápagos ho. *Geophys. J. Int.* 161, 763–788.
723 <https://doi.org/10.1111/j.1365-246X.2005.02592.x>
- 724 Segovia, M., Font, Y., Régnier, M., Charvis, P., Galve, A., 2018. Seismicity Distribution
725 Near a Subducting Seamount in the Central Ecuatorian Subduction Zone, Space-Time
726 Relation to a Slow-Slip Event. *Tectonics* 37, 2106–2123.
727 <https://doi.org/10.1029/2017TC004771>
- 728 Sladen, A., Trevisan, J., 2018. Shallow megathrust earthquake ruptures betrayed by their
729 outer-trench aftershocks signature. *Earth Planet. Sci. Lett.* 483, 105–113.
730 <https://doi.org/10.1016/j.epsl.2017.12.006>
- 731 Sokos, E.N., Zahradnik, J., 2008. ISOLA a Fortran code and a Matlab GUI to perform
732 multiple-point source inversion of seismic data. *Comput. Geosci.* 34, 967–977.
733 <https://doi.org/10.1016/j.cageo.2007.07.005>

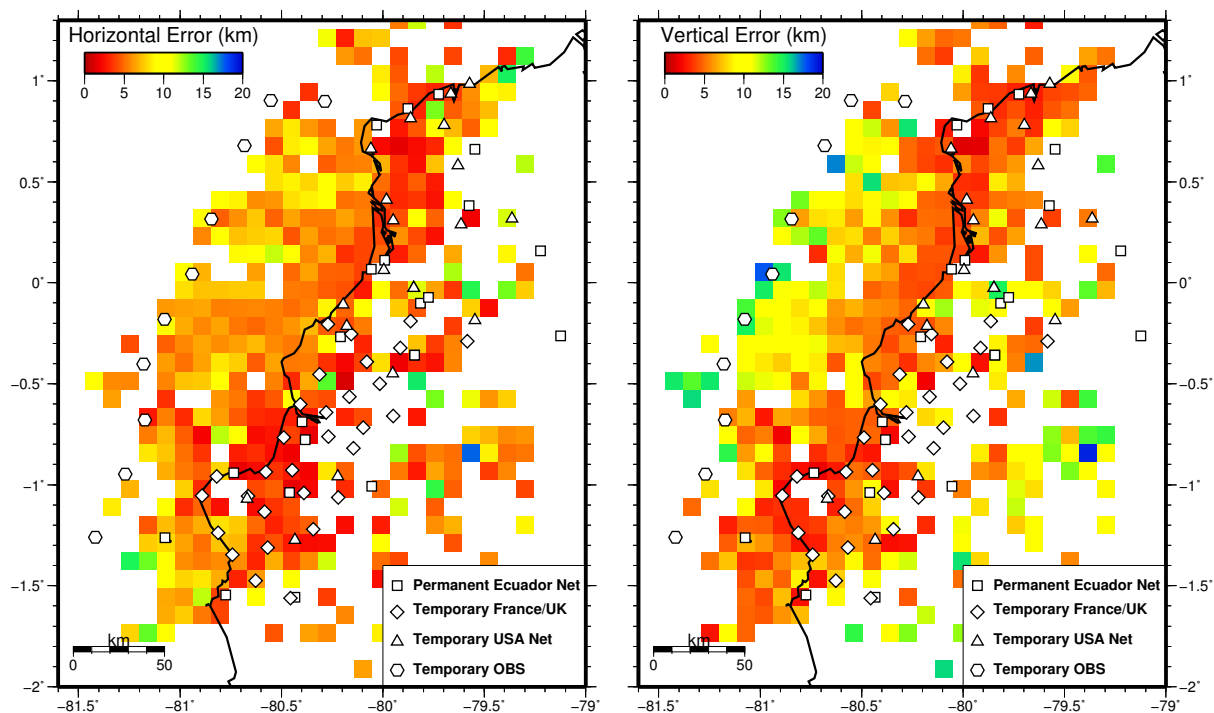
- 734 Soto-Cordero L., J. Nealy, A. Meltzer, H. Agurto-Detzel. A. Alvarado, S. Beck, H. Benz, E.
735 Bergman, P. Charvis, Y. Font, G. Hayes, S. Hernandez, M. Hoskins, S. Leon Rios, C.
736 Lynner, M. Regnier, A. Rietbrock, M. Ruiz, J. C. Stachnik, W. Yeck, 2017, New
737 insights on co- and post-seismic deformation and slip behavior associated with the
738 Mw7.8 2016 Pedernales, Ecuador earthquake and its aftershock sequence”, Abstract
739 [S53C-0715](#) presented at *2017 Fall Meeting, AGU*, New Orleans, LA, 11-15 Dec
- 740 Stein, R.S., 1999. The role of stress transfer in earthquake occurrence : Abstract : Nature.
741 Nature 402, 605–609.
- 742 Vaca, S., Vallée, M., Nocquet, J.M., Battaglia, J., Régnier, M., 2018. Recurrent slow slip
743 events as a barrier to the northward rupture propagation of the 2016 Pedernales
744 earthquake (Central Ecuador). *Tectonophysics* 724–725, 80–92.
745 <https://doi.org/10.1016/j.tecto.2017.12.012>
- 746 Vallée, M., Nocquet, J.M., Battaglia, J., Font, Y., Segovia, M., Régnier, M., Mothes, P.,
747 Jarrin, P., Cisneros, D., Vaca, S., Yepes, H., Martin, X., Béthoux, N., Chlieh, M., 2013.
748 Intense interface seismicity triggered by a shallow slow slip event in the Central
749 Ecuador subduction zone. *J. Geophys. Res. Solid Earth* 118, 2965–2981.
750 <https://doi.org/10.1002/jgrb.50216>
- 751 Waldhauser, F., Ellsworth, W.L., Schaff, D.P., Cole, A., 2004. Streaks, multiplets, and holes:
752 High-resolution spatio-temporal behavior of Parkfield seismicity. *Geophys. Res. Lett.*
753 31, L18608. <https://doi.org/10.1029/2004GL020649>
- 754 Wang, H.F., 2000. *Theory of Linear Poroelasticity*. Princeton Univ. Press., Princeton, N.J.
- 755 Wang, K., Bilek, S.L., 2014. Invited review paper: Fault creep caused by subduction of rough
756 seafloor relief. *Tectonophysics* 610, 1–24. <https://doi.org/10.1016/j.tecto.2013.11.024>
- 757 Wessel, P., Smith, W.H.F., 1998. New, improved version of generic mapping tools released.
758 *Eos, Trans. Am. Geophys. Union* 79, 579–579. <https://doi.org/10.1029/98EO00426>
- 759 Wetzler, N., Lay, T., Brodsky, E.E., Kanamori, H., 2018. Systematic deficiency of
760 aftershocks in areas of high coseismic slip for large subduction zone earthquakes. *Sci.*
761 *Adv.* 4, 1–9. <https://doi.org/10.1126/sciadv.aao3225>
- 762 Yabe, S., Ide, S., 2018. Why Do Aftershocks Occur Within the Rupture Area of a Large
763 Earthquake? *Geophys. Res. Lett.* 45, 4780–4787.
764 <https://doi.org/10.1029/2018GL077843>
- 765 Ye, L., Kanamori, H., Avouac, J.P., Li, L., Cheung, K.F., Lay, T., 2016. The 16 April 2016,
766 MW7.8 (MS7.5) Ecuador earthquake: A quasi-repeat of the 1942 MS7.5 earthquake and
767 partial re-rupture of the 1906 MS8.6 Colombia–Ecuador earthquake. *Earth Planet. Sci.*
768 *Lett.* 454, 248–258. <https://doi.org/10.1016/j.epsl.2016.09.006>
- 769 Yoshimoto, M., Kumagai, H., Acero, W., Ponce, G., Vásconez, F., Arrais, S., Ruiz, M.,
770 Alvarado, A., Pedraza García, P., Dionicio, V., Chamorro, O., Maeda, Y., Nakano, M.,
771 2017. Depth-dependent rupture mode along the Ecuador-Colombia subduction zone.
772 *Geophys. Res. Lett.* 44, 2203–2210. <https://doi.org/10.1002/2016GL071929>



775
776
777
778
779
780
781
782
783
784
785
786
787
788
789
790
791
792
793
794
795

Figure 1. Interseismic coupling (Nocquet et al., 2014) and main seismotectonic features. White stars and solid white lines show epicentres and approximate rupture areas of past megathrust earthquakes respectively (Kanamori and McNally, 1982; Mendoza and Dewey, 1984). Yellow star shows epicentre of 2016 mainshock together with its GCMT focal mechanism. Blue contour shows rupture area of 2016 event (Nocquet et al., 2017). Black contours show depth of subduction interface every 10 km (Hayes, 2012). Segmented black line indicates the Dolores-Guayaquil Fault Zone (Collot et al., 2002). Convergence NAZ/NAS from Chlieh et al. (2014). NAZ Nazca Plate, NAS North Andean Sliver, SAM South American Plate.

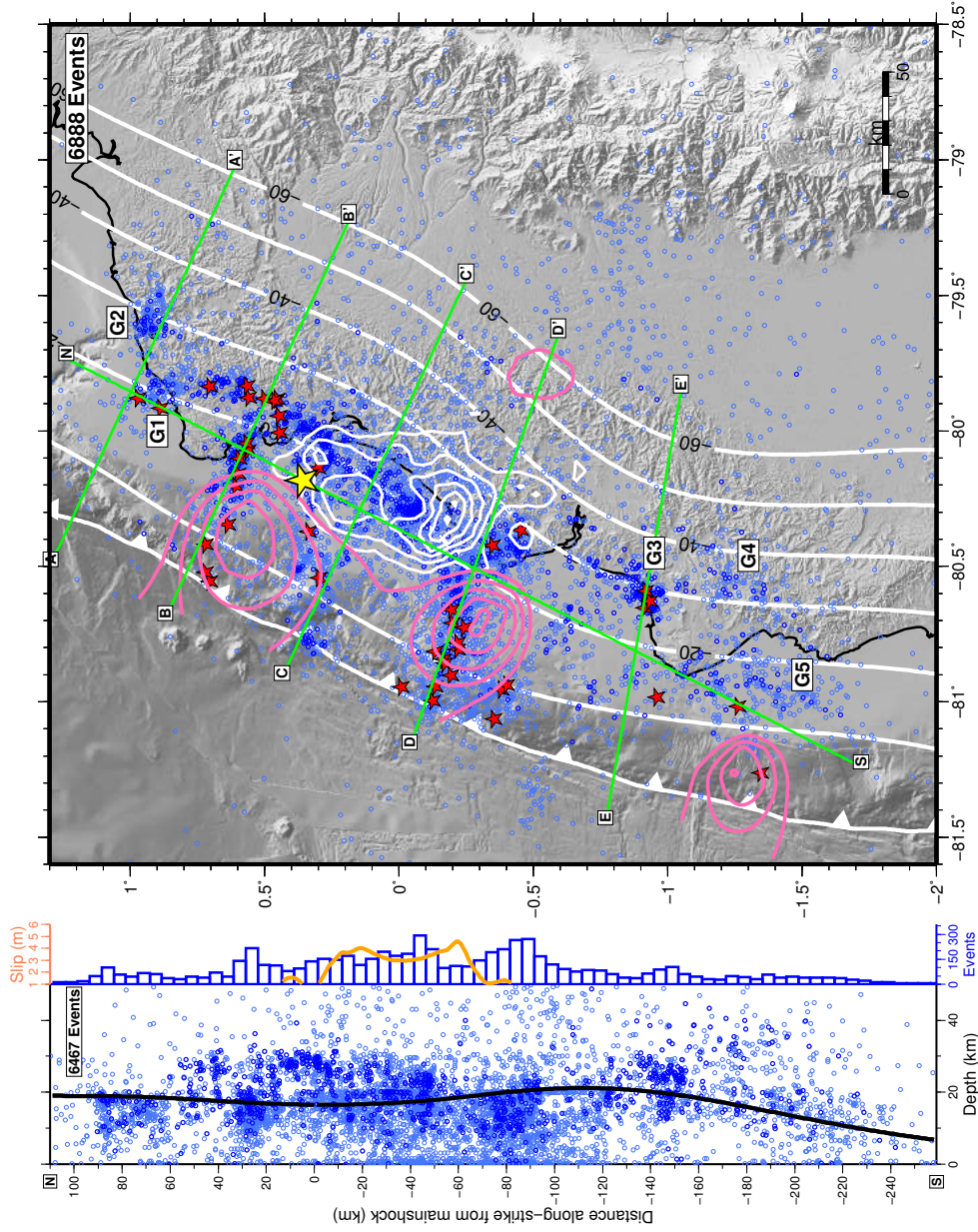
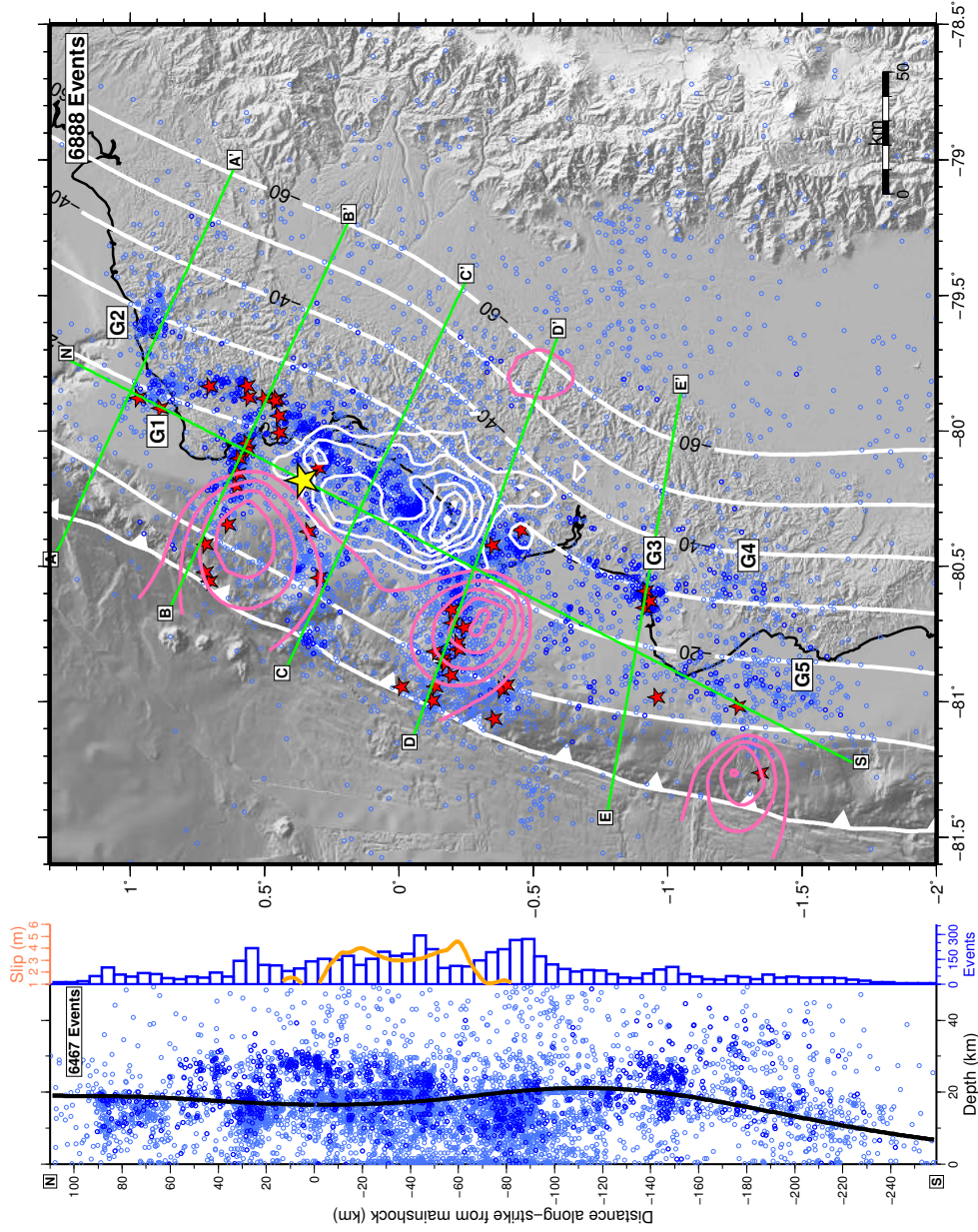
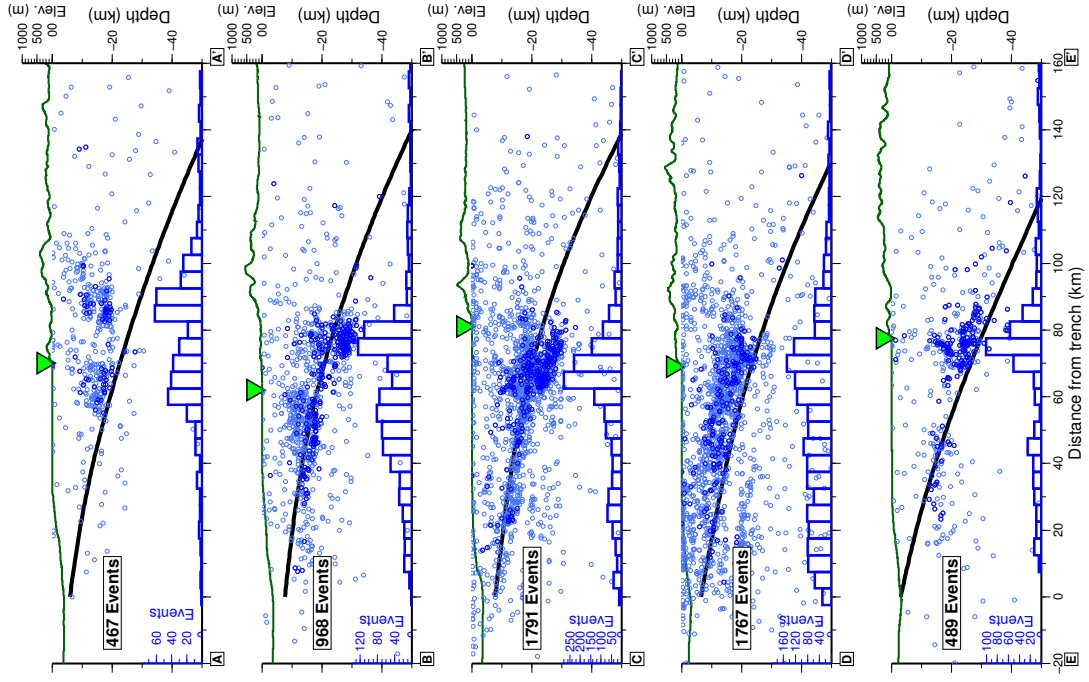
796
797



798
799

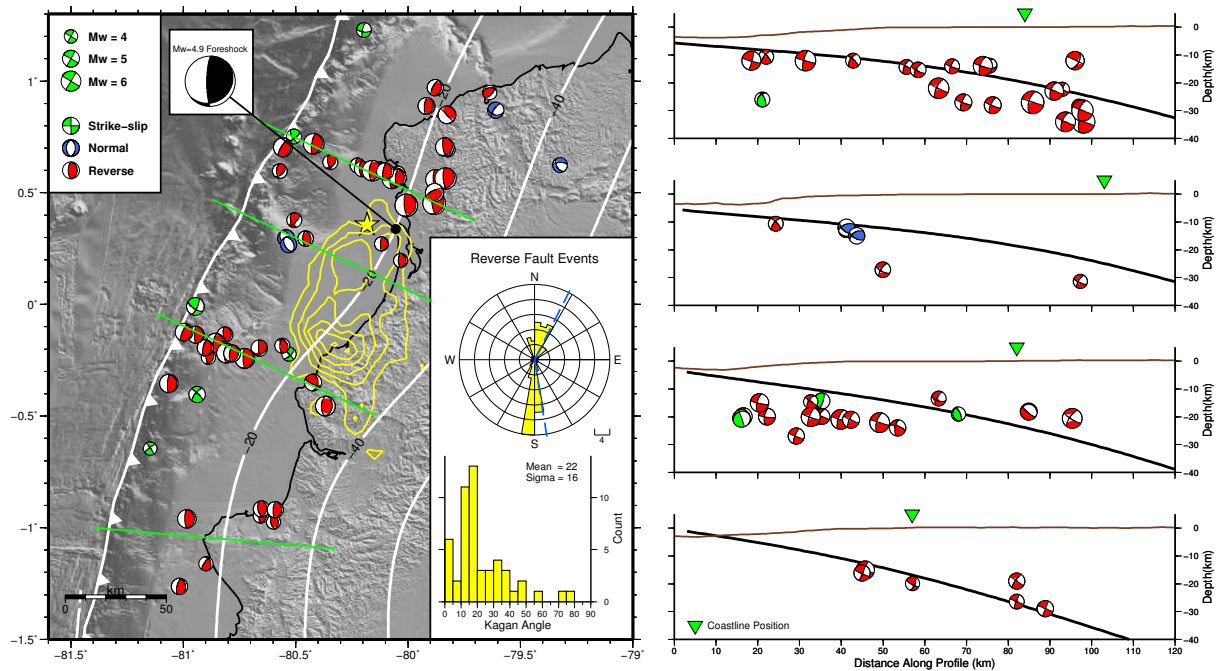
800 **Figure 2.** Seismic network and average location errors (68% confidence) for events with
801 confidence ellipse semi-axes less than 20 km (50% of total events). Left: average horizontal
802 error; Right: average vertical error.

803
804
805
806
807
808
809
810
811
812
813



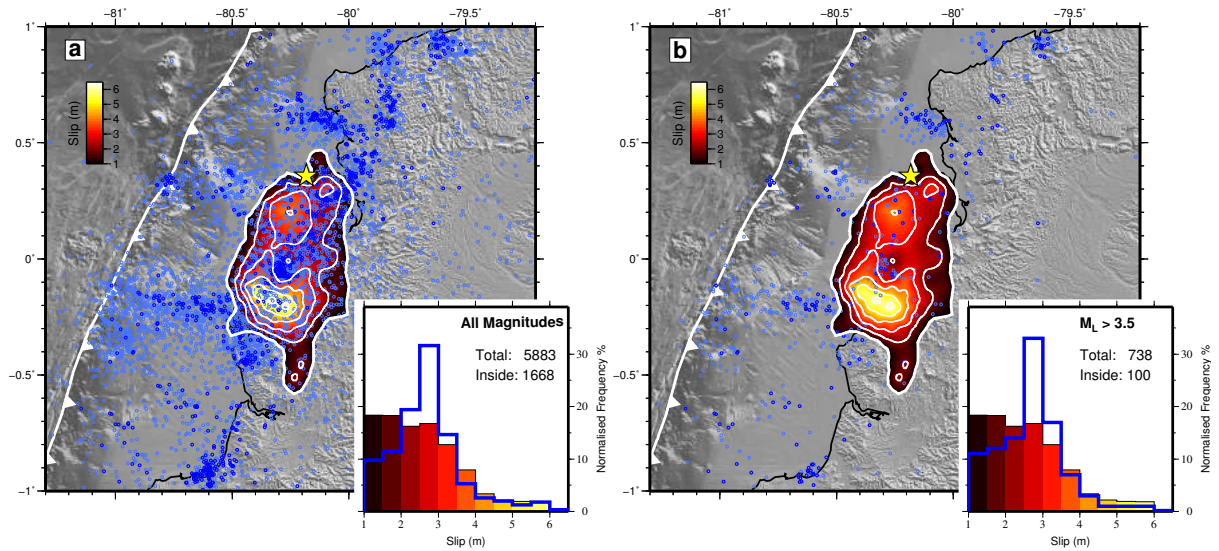
815
 816
 817
 818
 819
 820
 821
 822
 823
 824
 825
 826
 827
 828
 829
 830
 831
 832

Figure 3 (previous page). Aftershock locations in map view and depth sections. Light blue circles show all first quality locations; dark blue circles show high accuracy locations with ellipse semi-axis errors less than 5 km. Coseismic rupture model is shown as white contours every 1 m slip (Nocquet et al., 2017). Red stars are aftershocks with $M_L \geq 5$. Pink contours show afterslip every 10 cm (Rolandone et al., 2018). Clusters (G1-G5) indicate seismicity groups described in Section 3. Slab depth model (white lines in map, black line in depth sections) from Hayes, 2012. Histograms with blue bars show number of earthquakes for each profile. Histogram with orange line in N-S profile show distribution of coseismic slip along strike.



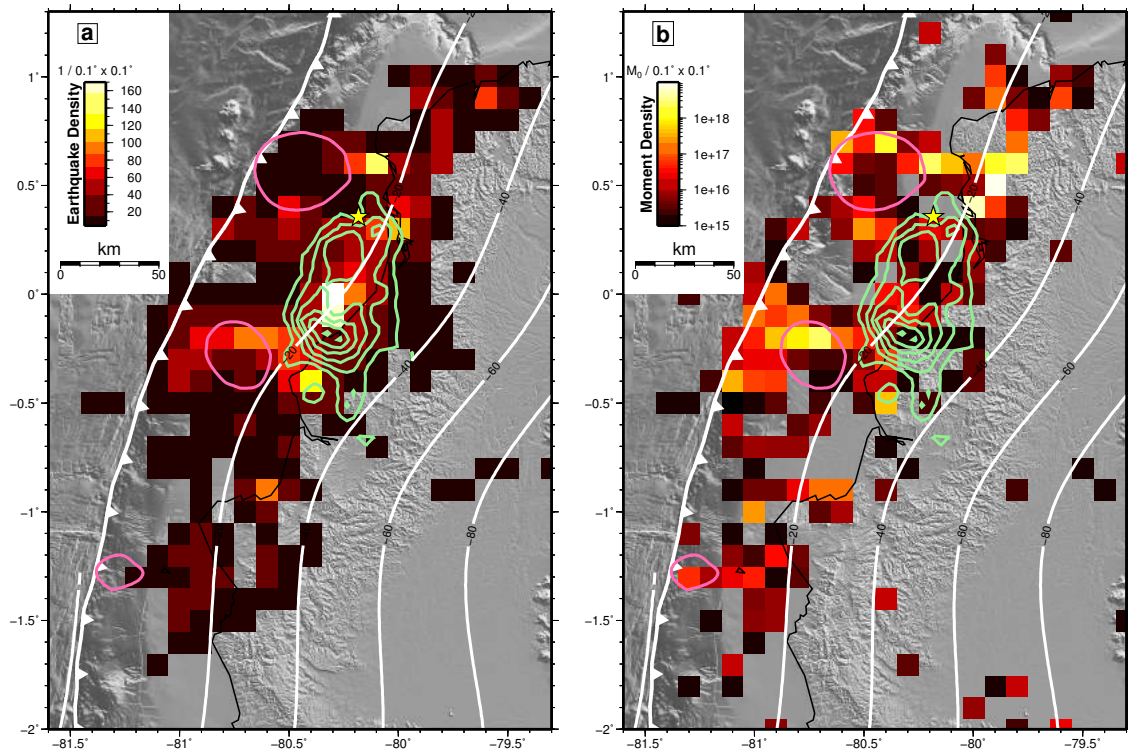
833
 834
 835
 836
 837
 838
 839
 840
 841
 842
 843
 844
 845
 846
 847

Figure 4. GCMT mechanisms and regional moment tensors obtained in this work. Distribution shows epicentral location from this study for all events, and depth from computed centroid depth. Inset (top) rose histogram showing strike of nodal planes for all reverse fault mechanisms. Blue segmented line shows strikes of nodal planes for mainshock. Inset (bottom) shows histogram of rotational angle relative to mainshock mechanism for all reverse fault events. For details, see also Table 2 in Supplementary Material.



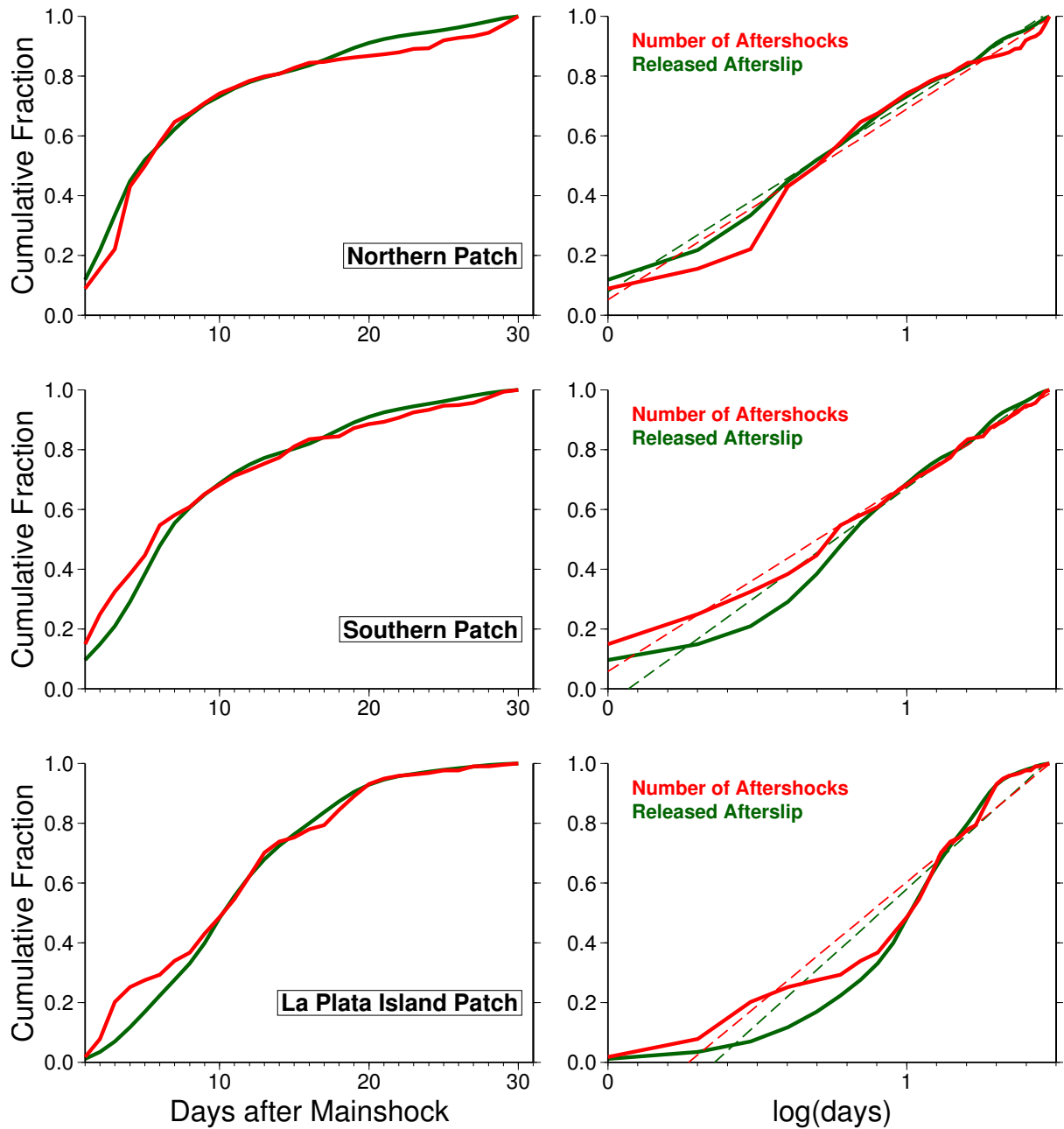
848
849
850
851
852
853
854
855
856
857
858

Figure 5. Distribution of aftershocks and coseismic rupture (Nocquet et al., 2017). (a) all magnitudes; (b) magnitudes equal or greater than 3.5. Histograms show normalized frequency distribution of coseismic slip (colour bars) and aftershocks (blue line).



859
860
861
862
863

Figure 6. Density plots for (a) number of earthquakes, (b) seismic moment. Other features same as in Fig. 2.

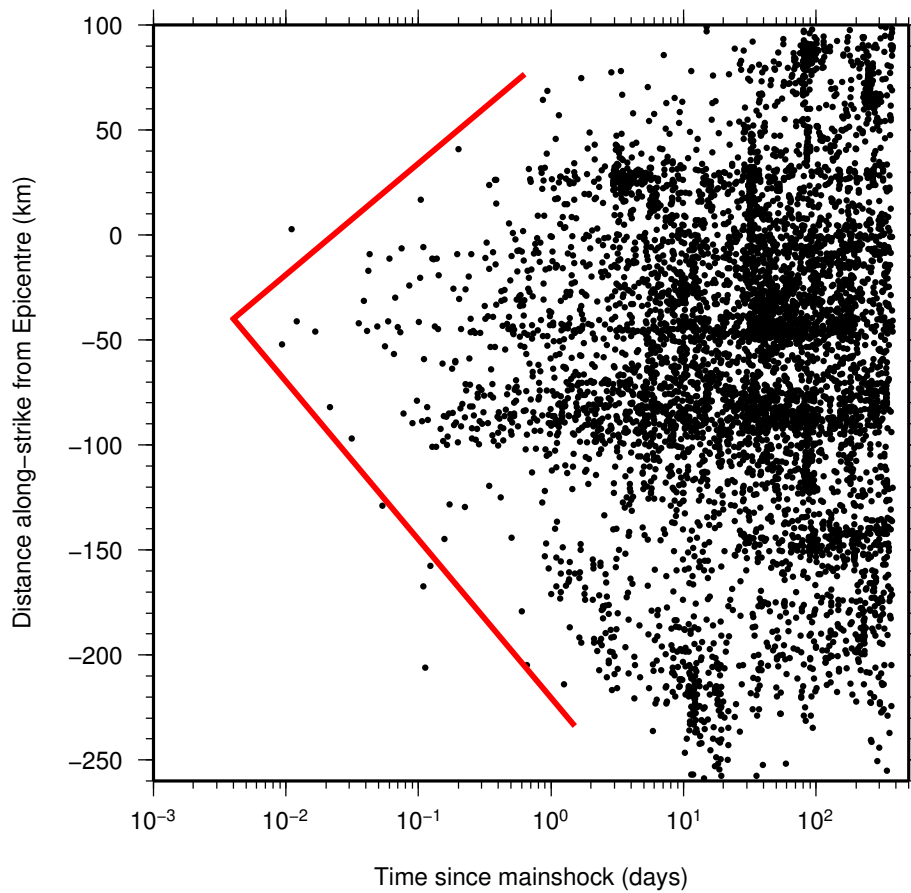


864
865

866 **Figure 7.** Temporal evolution of afterslip and aftershocks for the three different afterslip
867 patches during the first 30 days following the mainshock. Released afterslip distribution after
868 Rolandone et al. (2018). Left panels: cumulative distribution as a function of day. Right
869 panels: cumulative distribution as a function of logarithm of day. Segmented line is best-
870 fitted straight-line.

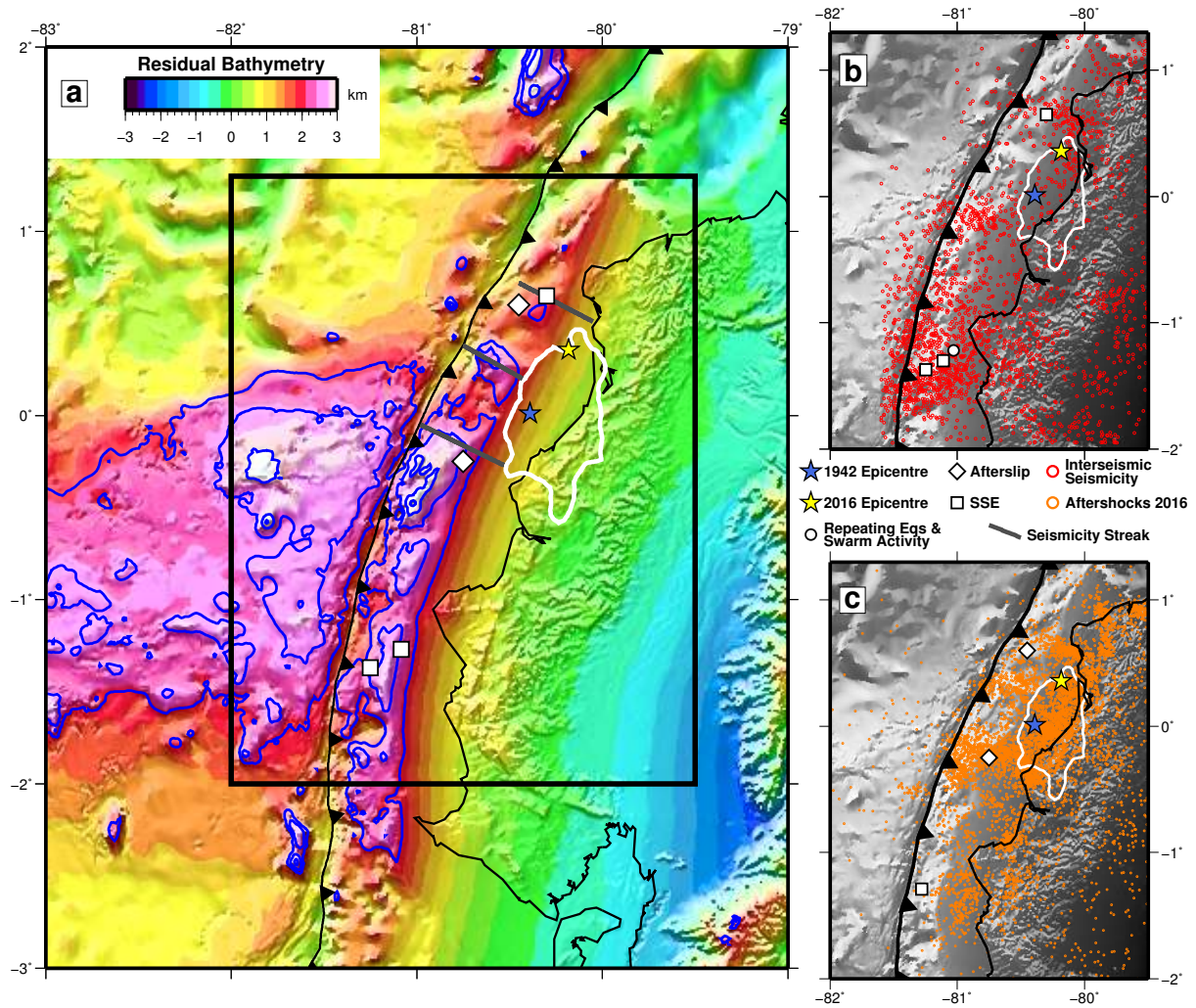
871
872
873
874
875
876
877
878

879
880



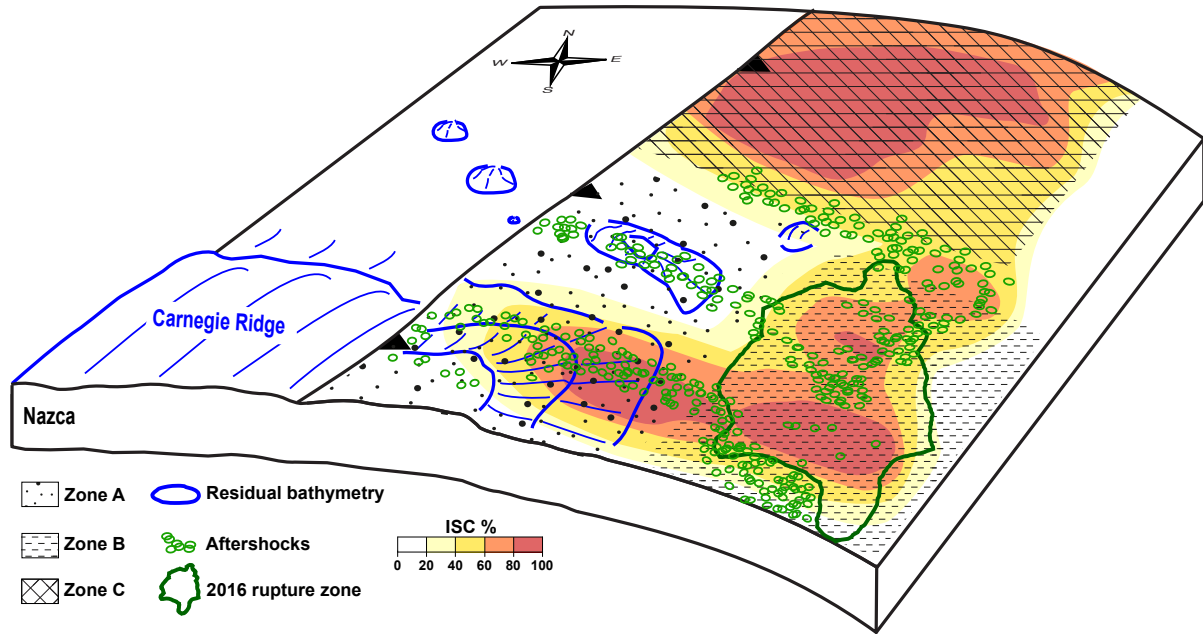
881
882
883
884
885
886
887
888
889
890
891
892
893
894
895
896
897
898
899
900
901
902
903
904
905

Figure 8. Expansion of earthquakes along strike in function of time since the mainshock. Red line indicates semi-logarithmic migration velocity of events (drawn by hand).



906
 907
 908
 909
 910
 911
 912
 913
 914
 915
 916
 917
 918
 919
 920
 921
 922
 923
 924
 925
 926
 927
 928

Figure 9. (a) Residual bathymetry and slip processes in the Ecuadorian margin. Blue contours every 500 m above 2000 m of residual bathymetry. Black box shows zoomed area in right-side panels. (b) interseismic (1943-2016) slip processes over residual bathymetry in grey scale. Seismicity from ISC catalogue. (c) postseismic slip processes (after 2016 mainshock) over residual bathymetry in grey scale.



930

931

932

933

934

935

936

937

938

939

940

941

942

943

944

945

946

947

948

949

950

951

952

953

954

955

956

957

Figure 10. Schematic summary figure. We propose that the area influenced by the subduction of the CR, as shown by the residual bathymetry contours, delimits the slip mode along dip and along strike in the Ecuadorian margin. Along dip, Zone A presents a rough and highly heterogeneous interface with the presence of fractures, possible fluids and overall low coupling. The interface at Zone A would be weak and seismically stable (velocity strengthening), and its slip mode is dominated by creeping, and includes SSE, repeating earthquakes, small to medium size ($M < 6$) earthquakes and swarm activity, including the permanent bands of seismicity. Down dip, Zone B is less influenced by the CR, presenting an overall high coupling and a smoother interface allowing for large megathrust ruptures, although contained within ~ 15 to 40 km depth as in the case of the 1942 and 2016 ruptures. North of the CR along strike, Zone C is out of the influence of the CR and presents overall high ISC and large ($M > 7.5$) megathrust ruptures that occasionally can reach the trench as in the case of the 1906 earthquake. The interfaces of both Zones B and C therefore would be unstable/conditionally stable (velocity weakening).